Computational Materials Science 231 (2024) 112605

Contents lists available at ScienceDirect

Computational Materials Science

journal homepage: www.elsevier.com/locate/commatsci

Full length article

# Predictive microstructure distribution and printability maps in laser powder bed fusion for a Ni–Cu alloy

Xueqin Huang [a,*], Raiyan Seede [a,d], Kubra Karayagiz [a,c], Austin Whitt [a], Bing Zhang [b], Jiahui Ye [b], Ibrahim Karaman [a], Alaa Elwany [a,b], Raymundo Arróyave [a,b]

[a] Department of Materials Science and Engineering, Texas A&M University, College Station, TX, USA
[b] Wm Michael Barnes '64 Department of Industrial and Systems Engineering, Texas A&M University, College Station, TX, USA
[c] Department of Mechanical Engineering, Worcester Polytechnic Institute, Worcester, MA, USA
[d] Materials Science Division, Lawrence Livermore National Laboratory, Livermore, 94550 CA, USA

ARTICLE INFO

*Keywords:*
Additive manufacturing
Laser powder bed fusion
Microstructure distribution
Phase field model
Printability map

ABSTRACT

The solidification microstructure of a melt pool under additive manufacturing conditions is highly heterogeneous due to the heterogeneity in the thermal spatio-temporal fields. This work combines a finite element (FE)-based thermal model with a phase field model (PFM) to predict microstructure distribution among the process parameter span in LPBF, which is strongly controlled by local thermal histories. The segregation distribution across the parameter space can be classified into four different microstructure distribution types: (i) fully planar, (ii) bottom dendritic, (iii) top dendritic, and (iv) fully dendritic. Also, the relationship between the thermal histories (the temperature gradient (G) and the growth rate (R)) variation induced by P and $\vec{V}$ and the microstructure distribution is clearly analyzed in the paper. For a Ni-20 at.%Cu alloy, the predicted microstructural distribution is verified experimentally. The parameter space is further divided into homogeneous and heterogeneous regions using the predicted area fraction of cellular–dendritic segregation across the melt pools. The process map is then used to build AM parts with homogeneous microstructures, where only planar microstructure is found experimentally. This methodology will aid in the exploitation of the alloy and processing space to identify alloy-process combinations that yield microstructurally-homogeneous, defect-free parts, provided an *unconditionally printable regime* can be identified.

## 1. Introduction

Additive manufacturing (AM) can create three-dimensional objects that are geometrically and topologically complex in a layer-by-layer fashion [1–5]. Laser powder bed fusion (LPBF) that leverages a laser beam on a bed of metallic powder to melt and fuse the material to form the three-dimensional part is one of the most common metal AM processes [6–8]. The common process parameters included in LPBF are laser power (P), scanning velocity ($\vec{V}$), hatch spacing, and layer thickness. AM has the potential to produce parts with highly precise and tailored properties, but a highly variable range of properties and performance can be found in AM-fabricated parts. This variability is often attributed to processing condition variations and the complex and difficult-to-control local thermal histories that occur during AM. This can lead to challenges in producing consistent and reliable parts using AM [9,10].

To produce consistent and high-quality parts using AM, it is important to understand the relationships between process parameters and microstructural heterogeneity. By selecting appropriate values for these parameters, it is possible to achieve desirable microstructures. However, microstructure variation in the form of solute element microsegregation can be caused by the complex thermal history distribution at the melt pool front, which is influenced by the processing conditions. This microstructural heterogeneity significantly impacts the performance of AM-fabricated prints. Understanding the links between process parameters and microstructural heterogeneity is critical for optimizing AM processes and producing reliable parts with consistent properties [11–13].

Many research groups have extensively studied the relationship between process parameters like P and $\vec{V}$ and the formation of microsegregated microstructures during AM. These investigations have aimed to understand how different processing conditions can influence the microstructural heterogeneity of AM-fabricated parts, and how this heterogeneity can be controlled to produce parts with consistent and desired properties [14–16]. Seede et al. examined the influence

* Corresponding author.
*E-mail address:* xueq13@tamu.edu (X. Huang).

https://doi.org/10.1016/j.commatsci.2023.112605
Received 26 June 2023; Received in revised form 9 October 2023; Accepted 23 October 2023
Available online 1 November 2023

of alloy composition and related phase diagrams on microstructure development in LPBF of four binary nickel-based alloys (Ni-20% Cu, Ni-5% Al, Ni-5% Zr, and Ni-8.8% Zr) [17]. They studied both single tracks and bulk parts. The researchers discovered that the primary dendritic arm spacing (PDAS) in AM components can be regulated by modifying P and $\vec{V}$, which in turn affect the local temperature gradient (G) and growth rate (R) conditions. Additionally, the solidification range and partition coefficient in the phase diagram were found to impact the amount and extent of solute segregation across the laser power-scan speed parameter space. This suggests that by carefully selecting process parameters and considering phase diagram features, it is possible to produce AM parts with a desired microstructure [17].

Microstructural evolution of specific alloy systems can be predicted using several approaches during LPBF in AM. These methodologies can help to optimize AM processes and improve the consistency and predictability of the resulting microstructures [18–28].

Karayagiz et al. demonstrated that a finite interface dissipation phase field model (PFM) coupled with a finite element (FE) thermal model could be used to predict the formation of dendritic microstructure in a Ni–Nb alloy system during AM. The FE thermal model implemented the finite element method to solve the heat transfer equation based on a reference frame of a heat source [29]. Steinbach et al. developed the finite interface dissipation PFM, which effectively describes both equilibrium and strongly non-equilibrium conditions. In their work, they introduced the notion of interface permeability to manage the atom transition between different phases [30]. In the integrated model, the FE model accepts P and $\vec{V}$ as inputs, and it outputs G and R at the melt pool. These values are then used as inputs for the PFM to predict the evolution of the microstructure. By considering the thermal history, including G and R at the interface between solid and liquid phases, this approach was able to accurately predict the microstructural evolution of the alloy, as validated by experimental observations. In regions with low linear energy density (LED), planar microstructures tend to dominate. Conversely, in areas with high LED, dendritic microstructures are more prevalent. Planar and cellular–dendritic microstructural formation in relation to G and R in L-PBF was investigated. In low R regions, planar microstructures are favored. As R increases, dendritic morphology begins to appear. However, if R continues to increase, planar microstructures eventually become dominant again. This methodology could potentially be used to optimize AM processes and improve the consistency and predictability of the resulting microstructures in this alloy system [31].

Wang et al. used a quantitative PFM to study the formation of Laves phase particles in a IN718 alloy system during AM. They found that a rich Ni concentration in the liquid phase, caused by a large angle between the G direction and the crystalline orientation, can suppress the formation of Laves phase particles due to its continuous long chain shape. This research suggests that hot cracking resistance can be improved at solidification sites with a large misorientation angle by controlling the Nb concentration in the liquid phase. This approach could potentially be used to optimize AM processes and improve the performance of IN718 alloy parts [32].

Sahoo et al. [33] used a PFM to study the relationship between cellular–dendritic grain growth and solidification parameters, such as G and R, in Ti–6Al–4V during AM. They found that dendrite arm spacing and $\vec{V}$ are negatively correlated. This research could potentially be used to optimize AM processes and improve the microstructural consistency of Ti–6Al–4V parts.

Finally, Huang et al. [34] developed a workflow for constructing "hybrid printability maps" that can predict defect-free and microstructure-homogeneous regions within P and $\vec{V}$ parameter space for Ni–Nb alloy parts produced through AM. These maps are constructed by calculating the fraction of the melt pool, under a particular set of processing conditions, that solidifies through a stable dendrite growth pattern. However, it is not yet fully understood how process parameter conditions control microsegregation within the melt pool. Further research is needed to explore the mechanisms that govern the microstructural distribution at the melt pool front.

Recent interest has been in identifying the optimal process parameter combinations for AM to produce parts with desirable microstructures and without macroscopic defects. Additionally, microstructure simulations have been developed to predict microstructural variation within a single melt pool. These efforts [29,31,33,35–37] have aimed to improve the consistency and predictability of AM processes and produce parts with improved properties.

Although significant progress has been made in understanding the relationships between process conditions, material properties, and microstructural variation in AM, a comprehensive framework for directly linking these factors within a single melt pool is still lacking. Currently, the effects of processing conditions are commonly studied using single-track scans, which examine how different combinations of laser parameters(i.e., P and $\vec{V}$) influence solidification conditions and, ultimately the microstructure distribution. Further research is needed to fully understand these relationships and develop a more comprehensive framework for predicting and controlling microstructural distribution in AM processes [17,37,38].

The microstructure distribution of single-track scans in AM can be classified into two main categories: homogeneous and heterogeneous. The microstructure distribution within the process parameter space can be further divided into four types: fully planar, bottom dendritic, top dendritic, and fully dendritic. Planar microstructures exhibit no microsegregation (Fig. 1(a)), whereas dendritic morphologies display microsegregation (Fig. 1(d)). Planar growth occurs due to solidification under equilibrium conditions, while dendritic growth arises when the liquid phase undergoes undercooling before the formation of the solid phase [39–41]. Understanding these microstructure distribution types and how process parameters influence them can help optimize AM processes and produce parts with consistent and desirable microstructures.

Micrographs showing examples of dendritic and planar structures within single track cross-sections for each of the four microstructure distribution types (*fully planar* microstructure/ *bottom dendritic* microstructure/ *top dendritic* microstructure/ *fully dendritic* microstructure) are presented in Fig. 1. These micrographs can help visualize the differences between the four types of microstructure distributions and how the process parameters influence them.

Fig. 1a shows a single track cross-section with a homogeneous microstructure consisting only of planar growth, which is an example of *fully planar* microstructure. The absence of a dendritic pattern indicates that the process parameters were selected to promote planar growth and produce a consistent microstructure throughout the melt pool. Fig. 1b shows a *bottom-dendritic* microstructure, where the top of the melt pool has a planar microstructure, and the bottom has a dendritic microstructure, as observed in SEM images. Fig. 1c shows a *top-dendritic* microstructure, where the top of the melt pool has a dendritic microstructure, and the bottom has a planar microstructure. Finally, Fig. 1d shows a *fully dendritic* microstructure, where dendrites are present across the entire melt pool. Understanding these different microstructure distributions and how process parameters influence them can help optimize AM processes and produce parts with consistent and desirable microstructures.

The selection of different microstructures in AM is related to local cooling conditions and the stable regions for dendritic or planar growth in temperature gradient-growth rate (G-R) maps. Fig. A.2 shows an example of a G-R map for Ni- 20 at. % Cu, where the combination of G and R falls within a triangular region demarcated by a purple line. The dendritic-planar boundary predicted by PFM separates dendritic and planar morphologies on the G-R map. A dendritic microstructure can be predicted if the (G, R) combination is within the triangular region. Otherwise, a planar microstructure is expected to form. The G-R map, which plots the G and R at the solid–liquid interface, can be used to predict the evolution of the material microstructure during

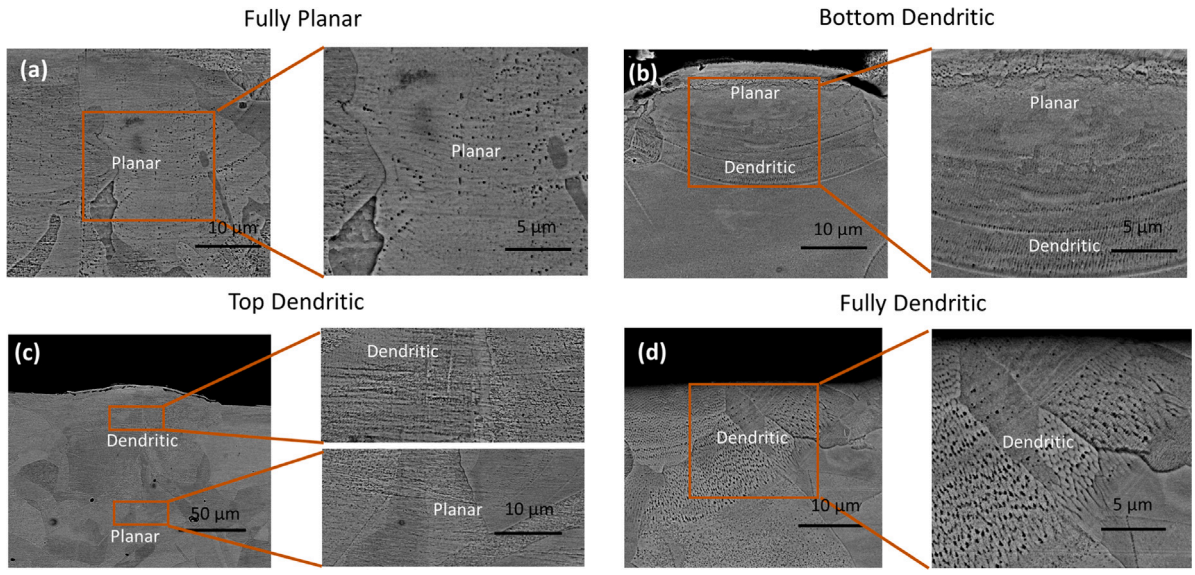


**Fig. 1.** Scanning Electron Microscopy (SEM) images for four representative microstructure distribution types and the corresponding magnified images of the melt pool cross-sections for Ni-20 at. % Cu: (a) fully planar, (b) bottom dendritic, (c) top dendritic, and (d) fully dendritic.

solidification. Different microstructures are selected based on the local cooling conditions, which can be influenced by the process parameters and the region of stability on the G-R map. By understanding these relationships and how they are affected by process parameters, it is possible to optimize AM processes and produce parts with consistent and desirable microstructures.

In this study, a finite element (FE) based thermal model and a finite interface dissipation phase-field model (PFM) were integrated to predict the distribution of the microstructure segregation in a Ni-20 at.% Cu alloy (as shown in Fig. 2). This study aimed to understand how process parameters influence the alloy's microstructural evolution during AM and optimize the AM process to produce parts with consistent and desirable microstructures.

The Ni–Cu alloy was chosen because it is relatively simple and has well-known thermophysical properties, making it easier to implement and deploy binary phase field models compared to more complex alloy systems. The results of the simulations were compared to experimental observations under nominally identical processing conditions, allowing for quantitative analysis of the microstructural evolution of the alloy under various process parameter combinations. By predicting the microstructure distribution, it is possible to optimize the AM process and produce parts with consistent and desirable microstructures.

In the integrated model, the melt local thermal history, such as temperature gradient ($G_{x,y,z,P,\vec{V}}$) and growth rate ($R_{x,y,z,P,\vec{V}}$), was defined as a function of position $(x, y, z)$ of the melt pool front, $P$, and $\vec{V}$. And G and R were predicted by the FE-based thermal model. The local microstructural type at the corresponding position $(x, y, z)$ was predicted by the finite interface dissipation PFM taking these combinations of the thermal history parameter ($G_{x,y,z,P,\vec{V}}$ and $R_{x,y,z,P,\vec{V}}$) as inputs. This integrated model can be used to predict microsegregation within the solidification front. The microstructure distribution type can be predicted based on the location of the dendritic pattern within the domain, with four typical microstructure types shown in Fig. 2. Additionally, a microstructure printability map can be generated based on the area fraction of dendritic microstructure, which is a function of the process parameters, reflecting the dominant microstructure type predicted over the cross-section longitudinally (the y–z plane projection of the melt pool front) of a single track.

In this work, we defined the microstructure printability map as the mapping, in the processing space of P and $\vec{V}$, of the degree of microsegregation under a given set of process conditions. While this map could also be referred to as a microstructure selection map, we specifically use the term "printability" to emphasize the fact that in AM, it is generally desirable to produce parts with as homogeneous a microstructure as possible, which can be achieved by selecting suitable process parameters. This avoids the need for additional post-processing steps that may result in coarsening of the printed microstructure or other detrimental effects. The microstructure printability map provides a valuable tool for optimizing the AM process and selecting process parameters that produce parts with consistent and desirable microstructures.

A finite element-based thermal model was combined with a finite interface dissipation phase-field model to predict the microstructure printability map for Ni-20 at.% Cu. The map was verified through single-track experiments by extensively exploring the process space. These experiments were followed by a detailed characterization of the solidified microstructure throughout the entire melt pool. This allowed for a comprehensive evaluation of the predicted microstructure distribution under various process conditions. The experimental results were then compared to the predictions made by the model, providing validation for the accuracy of the microstructure printability map in predicting microsegregation in this (model) Ni–Cu alloy system.

## 2. Experimental methodology

LPB-F Ni–Cu specimens were fabricated by using gas atomized Ni-20 at.%Cu powder(powder size range: 2-100μm, D50: 24.7 μm, D80: 51 μm) provided by Nanoval GmbH & Co. KG. A 3D Systems ProX DMP 200 system (fiber laser with a Gaussian profile $\lambda = 1070$ nm, and beam size = 80 μm) was used to print Single tracks. 10 mm length and 1 mm spacing between adjacent tracks were selected to print the tracks on a Ni-20 at.%Cu substrate under the industrial grade argon atmosphere with < 500 ppm oxygen content. Wire electrical discharge machining (EDM) was utilized to cut the cross-sections of the single tracks. Then the cross-sections were polished down to 0.25 μm with water-based diamond suspension polishing solutions. The Ni-20 at.%Cu single tracks were etched using Kalling's Solution No. 2 (5 g $CuCl_2$, 100 mL HCl, and 100 mL ethanol) to obtain optical micrographs.

A Keyence VH-X digital microscope equipped with a VH-Z100 wide-range zoom lens was used for Optical microscopy (OM). A CAMECA SXFive electron probe microanalyzer equipped with a LaB6 electron source was used to perform wavelength dispersive spectroscopy (WDS). A FEI Quanta 600 scanning electron microscope (SEM) was used to capture backscattered electron (BSE) images of polished single-track cross-sections. The settings to obtain the quantitative WDS composition

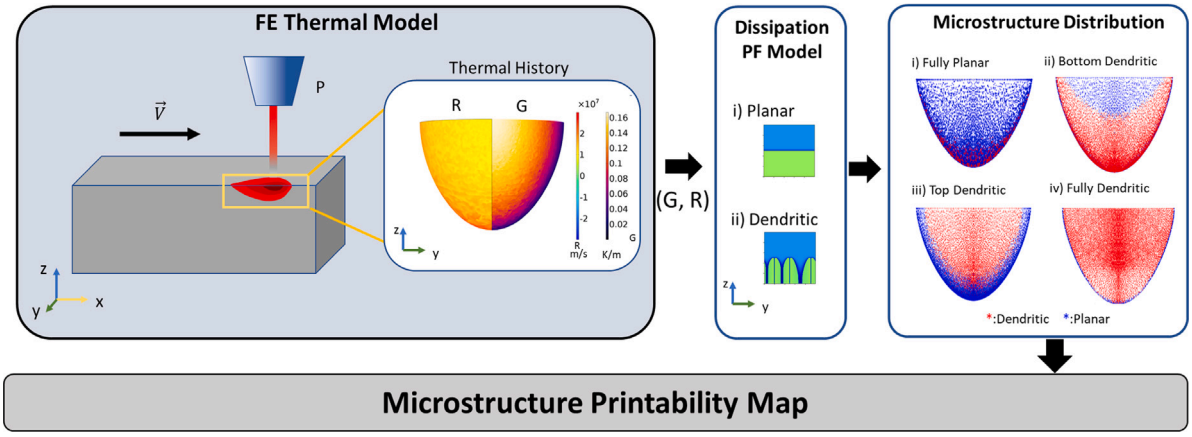


**Fig. 2.** Following is the workflow to predict a map of the microstructure printability in this study: A FE-based thermal model is utilized to predict the thermal history, including G and R, for each P and $\vec{V}$ combination. The microstructural evolution, microstructure distribution type, and fraction of dendritic microstructure across the melt pool are predicted by a finite interface dissipation PFM based on the thermal history. A printability map showing the microstructural segregation for the parameter space is generated by the area fraction of the dendritic microstructures across each melt pool cross-section predicted. This map can be used to identify regions of the parameter space that produce parts with desirable microstructures and can be utilized to optimize the AM process for a given material system.

maps were 15 kV, 100 nA, and 110 μs pixel dwell time with a 0.1 μm step size. The SEM images of the top center and the bottom of the melt pool and OM images are taken for three processing parameters (P = 71 W, $|\vec{V}|$ = 300 mm/s), (P = 71 W power, $|\vec{V}|$ = 50 mm/s), and (P = 212 W, $|\vec{V}|$ = 50 mm/s) to verify the microstructure distribution type and the melt pool dimension predicted by the integrated model.

## 3. Simulation methodology

The thermal history of different locations within the melt pool, including G and R, was calculated using the FE model for various combinations of P and $\vec{V}$. These values were then input into the PFM, which predicted the microstructural evolution and resulting microstructure distribution at each position within the melt pool. The spatial distribution of microstructure types (e.g., planar, dendritic) was obtained within the entire cross-section of the melt pool based on the local cooling conditions. The dendritic area fraction, calculated as the ratio of the area of the melt pool cross-section with dendritic growth to the total cross-section area, was used to obtain the microstructure printability map, mapping the degree of microsegregation in processing space (power-scan speed).

### 3.1. Finite element (FE) thermal model

For computational efficiency, a FE thermal model under a steady-state condition was utilized in this work, based on a reference frame of a heat source. We assume the heat source is moving with a constant velocity $\vec{V}$. Using the equation below, the heat transfer equation can be calculated:

$$\rho C_p(\nabla T \cdot \vec{V}) + \nabla(-k\nabla T) = Q \tag{1}$$

where $C_p$ is specific heat, $\rho$ is density and $k$ is thermal conductivity [29].

The heat transfer equation for the steady-state thermal model (Eq. (1)) includes a heat source term ($Q$) that accounts for vaporization, natural convection, surface radiation, and the deposited beam power. Eqs. (3) and (4) represent the radiation and convection terms, which are commonly used in FE thermal models for L-PBF. Eq. (5) shows the expression for the evaporative energy loss, while Eq. (6) refers to the beam deposition energy [29]. The latter also incorporates adjustments that consider both mass transport and energy transport within the vapor phase [29]. Eq. (5) adheres to the Bolten-Block/Eagar model with slight modifications to include temperature-dependent partial pressure relationships, as computed by the equations detailed in Ref. [42]. Conversely, Eq. (6) contains a phase-dependent absorptivity term, enabling the integration of keyhole formation without considering expensive fluid dynamics [29].

$$Q = q_{rad} + q_{conv} + q_{vap} + q_{beam} \tag{2}$$

$$q_{rad} = \varepsilon\sigma_B(T_{amb}^4 - T^4) \tag{3}$$

$$q_{conv} = h(T_{amb} - T) \tag{4}$$

$$q_{vap} = L_v \sum_{i=1}^{n} X_i 44.331 p_i(T)\sqrt{\frac{MW_i}{T}} \tag{5}$$

$$q_{beam} = a(T)P\left[\frac{1}{2\pi\sigma^2} exp\left(-\frac{(r-r_0)^2}{2\sigma^2}\right)\right] \tag{6}$$

According to whether the parameter depends on the temperature or the phase, the parameters in Eqs. (1)–(6) can be divided into two general categories, the temperature/phase-dependent properties, and the temperature/phase- independent properties. The temperature/phase-independent parameters include molecular weights of each element ($MW_i$), the Stefan–Boltzmann constant ($\sigma_B$), ambient temperature ($T_{amb}$), and emissivity ($\varepsilon$), as well as laser process parameters including centerpoint ($r_0$), standard deviation ($\sigma$), $P$, and $\vec{V}$. These parameters are assumed to be constant. The temperature/phase-dependent parameters consist of the partial pressure of each element ($p_i$), thermal conductivity ($k$), specific heat ($C_p$), absorptivity ($a$), and density ($\rho$). h is the natural convection coefficient. Table 1 displays the details of the phase-independent parameters, while Table 2 presents the phase-dependent parameters in detail implemented in the FE thermal model. The finite element method is implemented using COMSOL with a mesh size of 1 μm, which is fine enough to capture the physics near the laser beam region [29]. Based on the surface orientation and shape, COMSOL is used to calculate h [43].

After obtaining the temperature profile in the melt pool, G and R are calculated by the following equations [31]:

$$G = \sqrt{\left(\frac{\partial T}{\partial x}\right)^2 + \left(\frac{\partial T}{\partial y}\right)^2 + \left(\frac{\partial T}{\partial z}\right)^2} \tag{7}$$

$$R = |\vec{V}| \cdot \cos\theta \tag{8}$$

where $\theta$ is the angle between the normal vector of the solidification front and the scanning velocity.

### 3.2. Finite interface dissipation(FID) phase field model

The microstructure printability map shows the degree of heterogeneity, measured as the dendritic microstructure area fraction, of the

**Table 1**
Phase-independent thermo-physical parameters implemented in the FE thermal modeling of the Ni-20 at.%Cu investigated in this work.

| Phase ($i$) | Parameters | Source |
|---|---|---|
| $T_{amb}$ [K] | 298 | [31] |
| $4\sigma_B$ [μm] | 70 | Manuf. |
| $MW_{Cu}$ [g/mol] | 63.546 | [44] |
| $MW_{Ni}$ [g/mol] | 58.7 | [44] |
| $\epsilon$ | 0.07 | [29] |
| $P$ [W] | 60–250 | User |
| $\vec{V}$ [mm/s] | 50–2400 | User |

**Table 2**
Phase-dependent thermo-physical parameters implemented in the FE thermal modeling of the Ni-20 at.%Cu investigated in this work.

| Phase ($i$) | Solid ($S$) | Liquid ($L$) | Vapor ($V$) |
|---|---|---|---|
| $\rho_i$ [kg/m$^3$] | 8910 [45] | 8450 [45] | $\rho(T)$ |
| $C_p^i$ [J/kgK] | 520 [46] | 746.4 [46] | $C_p(T)$ |
| $\alpha_i$ [unitless] | 0.45[29] | 0.45[29] | 0.45[29] |
| $k_i$ [W/mK] | 100[47] | 130 [47] | 5 [29] |
| $k_{iz}$ [W/mK] | | | 3000[29] |
| $p_i$ [Pa] | | | p(T) |
| Transform. ($t$) | Solid ↔ Liquid ($m$) | Liquid ↔ Vapor ($v$) | |
| $T_t$ [K] | 1670[45] | 2902[45] | |
| $\Delta T_t$ [K] | 50[29] | 200[29] | |
| $L_t$ [kJ/kg] | 241[47] | 5773[47] | |

longitudinal cross-section of the melt pool at a given set of processing conditions. This is calculated using an integrated model that couples the FE thermal model and the finite interface dissipation PFM. The FE thermal model predicts the thermal history parameters, such as G and R, at the solidification fronts, which are then projected onto a two-dimensional plane (the y–z plane in Fig. 2) to produce the 2D $(G, R)$ combinations at the longitudinal cross-section of the melt pool. The G and R values are used as inputs for the finite interface dissipation PFM in order to determine the microstructure morphology at the corresponding position of the melt pool cross-section.

The simulations of the microstructure evolution are conducted for Ni-20 at.%Cu via PFM, developed by Steinbach et al. [30,48]. The grid spacing is set to 8 nm, and the domain size is 2000 × 2000 in this work [31]. An order parameter, $\phi$, is included in PFM, representing the pure liquid phase when $\phi$ is equal to 0 and the pure solid phase when $\phi$ is equal to 1. PFM also includes fields describing composition and temperature. The total Gibbs free energy can be expressed by [30]:

$$\begin{aligned} F &= \int_\Omega \left\{ f^{\text{intf}} + f^{\text{chem}} \right\}, \\ f^{\text{intf}} &= \frac{4\sigma_{\alpha\beta}}{\eta}\left\{ -\frac{\eta^2}{\pi^2}\nabla\phi_\alpha \cdot \nabla\phi_\beta + \phi_\alpha\phi_\beta \right\}, \\ f^{\text{chem}} &= \phi_\alpha f_\alpha\left(c_\alpha\right) + \phi_\beta f_\beta\left(c_\beta\right) + \lambda\left\{c - \left(\phi_\alpha c_\alpha + \phi_\beta c_\beta\right)\right\}. \end{aligned} \tag{9}$$

where $\eta$ is the interface width and $\sigma_{\alpha\beta}$ is the interface energy. The Lagrange multiplier $\lambda$ can be determined assuming that the equilibration achieves between two phases inside a reference volume RV and $\lambda$ is given by [30]:

$$\lambda = \phi_\alpha \frac{\partial f_\alpha}{\partial c_\alpha} + \phi_\beta \frac{\partial f_\beta}{\partial c_\beta} - \frac{\dot{\phi}_\alpha c_\alpha + \dot{\phi}_\beta c_\beta}{P} \tag{10}$$

The concentration evolution equations of $a$ and $\beta$ phases, $c_a$ and $c_\beta$, are as follows:

$$\phi_a \dot{c_a} = \nabla(\phi_a D_a \nabla c_a) + P^{intf}\phi_a\phi_\beta\left(\frac{\partial f_\beta}{\partial c_\beta} - \frac{\partial f_a}{\partial c_a}\right) + \phi_a\dot{\phi_a}(c_\beta - c_a) \tag{11}$$

$$\phi_\beta \dot{c_\beta} = \nabla(\phi_\beta D_\beta \nabla c_\beta) - P^{intf}\phi_a\phi_\beta\left(\frac{\partial f_\beta}{\partial c_\beta} - \frac{\partial f_a}{\partial c_a}\right) - \phi_\beta\dot{\phi_\beta}(c_\beta - c_a) \tag{12}$$

**Table 3**
Material parameters used in the PF simulations.

| Parameter ($i$) | Values ($S$) |
|---|---|
| Grid spacing, $\Delta x$ (nm) | 8 [31] |
| Interface width, $\eta$ (nm) | 32 [31] |
| Molar volume, $V_m$ (cm$^3$/mol) | 6.6 [45] |
| Interface energy, $\sigma_{a\beta}$ (J/cm$^2$) | 1 ×10$^{-5}$ [31] |
| Interface mobility, $\mu_{a\beta}$ (cm$^4$/Js) | 2 |
| Diffusivity of solid, $D_S$ (cm$^2$/s) | 1.0 ×10$^{-9}$ [45] |
| Diffusivity of liquid, $D_L$ (cm$^2$/s) | 1.0 ×10$^{-5}$ [45] |
| Interface permeability, $P^{intf}$ (cm$^3$/Js) | 50 000 |

where $D_a$ and $D_\beta$ are the chemical diffusivity for $a$ phase and $\beta$ phase, separately, $f_a$ and $f_\beta$ are the free energy densities of phase $a$ and $\beta$, respectively, generated by the CALPHAD database, and $P^{intf}$ is the interface permeability coefficient [45]. $P^{intf}$ in this work can be derived by $\frac{8M}{a\eta}$ [30]. And the lattice constant, a, is $3 \times 10^{-8}$ cm, and the mobility, M, can be estimated according to $D_\alpha = \frac{MRT}{V_m}$ [31]. Since $D_\alpha$ can be $D_L$ and $D_S$, the range of M value can be between $10^{-12}$ and $10^{-9}$ cm$^5$/Js. M is selected to be $6 \times 10^{-10}$ cm$^5$/Js in this work. Therefore, $P^{intf}$ for Ni-20 at.% Cu is 50 000 cm$^5$/Js. The CALPHAD formalism is used to define the free-energy densities for the liquid phase and the solid phase [49]:

$$\begin{aligned} f_\alpha V_m = {} & c_\alpha G^0_{Nb} + \left(1 - c_\alpha\right) G^0_{\text{Cu}} \\ & + k_c T\left(c_\alpha \ln\left(c_\alpha\right) + \left(1 - c_\alpha\right)\ln\left(1 - c_\alpha\right)\right) \\ & + c_\alpha\left(1 - c_\alpha\right)\sum_{i=0}^{n} G_i\left(2c_\alpha - 1\right)^i \end{aligned} \tag{13}$$

where $Vm$, $k_c$, and $T$ represent the molar volume, ideal gas constant, and temperature, respectively. $G^0_{\text{Ni}}$, $G^0_{\text{Cu}}$ are reference states of constituent elements. $G_i$ terms are coefficients contributing to excess Gibbs energy. The coefficients for each phase are obtained from [47].

The phase field evolution equation can be derived as following [30]:

$$\begin{aligned} \dot{\phi}_\alpha &= -\frac{\pi^2}{8\eta}\mu_{\alpha\beta}\left\{\frac{\delta F}{\delta\phi_\alpha} - \frac{\delta F}{\delta\phi_\beta}\right\} \\ &= \mu_{\alpha\beta}\left\{\sigma_{\alpha\beta}\left[\nabla^2\phi_\alpha + \frac{\pi^2}{\eta^2}\left(\phi_\alpha - \frac{1}{2}\right)\right] - \frac{\pi^2}{8\eta}\Delta\tilde{g}_{\alpha\beta}\right\} \end{aligned} \tag{14}$$

where

$$\Delta\tilde{g}_{\alpha\beta} = f_\alpha - f_\beta - \left(\phi_\alpha\tilde{\mu}_\alpha + \phi_\beta\tilde{\mu}_\beta - \frac{\dot{\phi}_\alpha\left(c_\alpha - c_\beta\right)}{P}\right)\left(c_\alpha - c_\beta\right) \tag{15}$$

By rearranging Eq. (14), the order parameters of the finite interface dissipation PFM can be expressed as:

$$\dot{\phi_a} = K\{\sigma_{a\beta}[\nabla^2{\phi_a}^2 + \frac{\pi^2}{\eta^2}(\phi_a - \frac{1}{2})] - \frac{\pi^2}{8\eta}\sqrt{\phi(1-\phi)}\Delta g^{\phi}_{a\beta}\} \tag{16}$$

$$K = \frac{8P^{inf}\eta\mu_{a\beta}}{8P^{inf}\eta + \mu_{a\beta}\pi^2(c_a - c_\beta)^2} \tag{17}$$

$$\Delta g^{\phi}_{a\beta} = f_a - f_\beta + (\phi_a\frac{\partial f_a}{\partial c_a} - \phi_\beta\frac{\partial f_\beta}{\partial c_\beta})(c_\beta - c_a) \tag{18}$$

where $\mu_{a\beta}$ is the interfacial mobility, $K$ is the kinetic coefficient describing the impact of solute "jump" between phases, and $\Delta g^{\phi}_{a\beta}$ is the chemical driving force.

The frozen temperature approach is implemented to simplify the model and further speed up the prediction process. The temperature evolution equation can be written as:

$$T(y) = T_0 + G(|\vec{n}| - Rt) \tag{19}$$

where $\vec{n}$ is along with the solidification direction, and $T_0$ is the reference temperature. Table 3 shows the detailed parameters used in the PFM simulation.

### 3.3. Boundary between the dendritic and the planar microstructure in G-R map

FID was used to predict the boundary between the dendritic and the planar microstructure in G-R map [31]. The thermal history, G and R, are the input for FID, and the microstructure for the given (G,R) combination can be predicted by FID. Therefore, the connection between the microstructure morphology and the thermal history can be built. Fig. A.1(a) displays the concentration profile for Cu, and Fig. A.1(b) denotes the Cu concentration varies along the x direction, as indicated by the red dash line in Fig. A.1(a). In Fig. A.1(b), $C_{int}$ represents the concentration between the cell cores. $C_s$ corresponds to the concentration within the cell core. When $\frac{(C_{int}-C_s)}{C_s}$ falls below 0.1%, the microstructure is considered to be planar; otherwise, it is recognized as dendritic.

In Fig. A.2, 49 G and R combinations (G ranging from $10^5$ K/m to $10^8$ K/m and R ranging from $10^{-3}$ m/s to 1 m/s) was selected to roughly estimate the range of the planar-to-dendritic and dendritic-to-planar transition growth rate for a given G. We also selected 30 additional (G, R) combinations to more accurately locate the transition growth rate within the previous 49 data points. The predicted planar microstructure is indicated by blue square symbols, while the predicted dendritic microstructure is indicated by red triangle symbols in Fig. A.2. The (G, R) combinations selected to predict the dendritic-planar boundary are shown by the purple line in Fig. A.2. The planar and dendritic boundary (red line) was generated to ensure that only dendritic morphologies can be predicted within the triangle region surrounded by the dendritic-planar boundary in G-R map by the FID model. In contrast, exclusively planar morphologies can be predicted outside the triangle region surrounded by the dendritic-planar boundary in the G-R map.

### 3.4. The microstructure distribution

The thermal history, or (G, R) distribution, at the front of the melt pool, can be calculated using a finite element thermal model. Based on the (G, R) distribution across the entire melt pool, the corresponding microstructure can be predicted using a phase field model. This allows us to obtain the microstructure distribution across the whole melt pool front. After the microstructure pattern within the melt pool cross section is obtained, we can classify the microstructure distribution on the basis of the presence and location of dendritic microstructures. If no dendritic microstructure is predicted in the entire melt pool, the microstructure distribution is defined as “fully planar.” If the dendritic microstructure is located mainly at the bottom of the melt pool, the microstructure distribution is defined as “bottom dendritic.” Moreover, the dendritic microstructure is mainly located at the melt pool top part; the microstructure distribution is defined as “top dendritic”. Finally, if dendritic microstructures are present throughout the entire melt pool, the microstructure distribution is defined as “fully dendritic”.

### 3.5. Dendritic area fraction(FD)

As mentioned, the microstructure of the melt pool can be quantified by the area fraction occupied by dendritic microstructures at the longitudinal cross-section of the melt pool. For instance, when this fraction is zero, fully planar microstructures are present at the melt pool front, which corresponds to a case where planar growth is dominant. The dendritic area fraction ($FD$) is calculated using the following equation:

$$FD = \frac{A_D}{A_{total}} \tag{20}$$

where $A_D$ is the area where dendritic microstructures are found within the longitudinal cross-section of a melt pool, and $A_{total}$ is the total area of the longitudinal cross-section of the melt pool.

We use an approximate method to calculate the dendritic area fraction ($FD$). First, we use a finite element thermal model to predict the microstructure at each grid point in the domain using a mesh with a size of 1 micrometer. A value of 0 is allocated to the grid when a planar microstructure is predicted, whereas a value of 1 indicates a prediction of dendritic microstructure. However, because we use the finite element method to analyze a three-dimensional domain in COMSOL, there is no direct relationship between the number of data points and the area they represent. To establish this relationship, we subsample several data points inside the melt pool on a grid of 0.1 μm by 0.1 μm. We then used a K-Nearest Neighbors(KNN) function with six neighbors in Matlab to interpolate the microstructure type of the sampled points based on the data predicted by the integrated model [50]. KNN uses the melt pool position as input, and its output labels correspond to the microstructure morphology, either planar or dendritic. Fig. A.3(a) indicates the microstructure morphology predicted directly by the integrated model, coupling the phase field model and the thermal model [31]. The blue color represents the planar microstructure, while the red color indicates the dendritic microstructure. Note that the data point distribution in the melt pool is non-uniform due to the adaptive mesh. Fig. A.3(b) shows the microstructure distribution predicted by KNN on 0.1 μm-by-0.1 μm mesh. Comparing Fig. A.3(a), Fig. A.3 (b) can determine the microstructure morphology uniformly on the melt pool. In Fig. A.3(b), we obtain the number of subsampled points with dendritic microstructure $n_d$ (red symbols) and the total number of subsampled points $n_t$(red symbols and blue symbols). $\frac{n_d}{b_t}$ s a good approximation for $\frac{A_D}{A_{total}}$, or FD.

## 4. Results and discussion

In this section, we show the thermal history (G and R) distribution throughout the melt pool for low, medium, and high LED. Two processing parameters are selected for the low, and the high LED cases and two processing parameters are chosen for the medium LED showing top-dendritic and bottom-dendritic morphology, since LED is a suitable processing parameter to control the material properties [29,51,52]. LED is defined as:

$$\text{LED} = \frac{P}{|\vec{V}|} \tag{21}$$

We also show each LED’s corresponding microstructure distribution type and compare it with experimental results. Furthermore, we investigate the relationship between the thermal history distribution and the microstructure distribution. Finally, we present a microstructure printability map for Ni-20 at.%Cu, which predicts the homogeneous and heterogeneous regions in the process parameter range based on experimental results.

To understand the physical underpinnings for the formation of the different microstructure distribution types, the effect of the thermal histories distribution on the microstructure distribution is investigated first in the case corresponding to the low LED condition in Fig. 3. We define $x$ as the coordinate along the melt pool width direction, while $y$ corresponds to the coordinate along the melt pool depth direction. The origin is located at the top center of the melt pool. Since every position $(x, y)$ in the melt pool cross-section has its corresponding local thermal history ($G(x, y)$ and $\mathrm{R}(x, y)$), we plot the G-R maps with color indicating positions in Fig. 3(a) and 3(c) to visualize how the local thermal histories affect the local microstructure in Fig. 3(b) and 3(d). Thus, the color of the points in the G-R map (Fig. 3(b))indicates the $x$ position within the molten pool (Fig. 3(a)), while the color of the points in the G-R map (Fig. 3(d)) denotes the $y$ position within the molten pool (Fig. 3(c)).

The position-dependent G and R for the low LED case are shown in Fig. 3(b) and (d). The red line in the G-R map represents the dendritic-planar boundary, calculated using the FID model. Fig. 3(e) displays the predicted microstructure distributions at the melt pool cross-section with low LED. The red points indicate the dendritic microstructure is predicted at the melt front position $(x, y)$, while the blue points represent a planar microstructure. Fig. 3(e) shows a fully-planar microstructure distribution from the prediction with parameters P = 94 W,

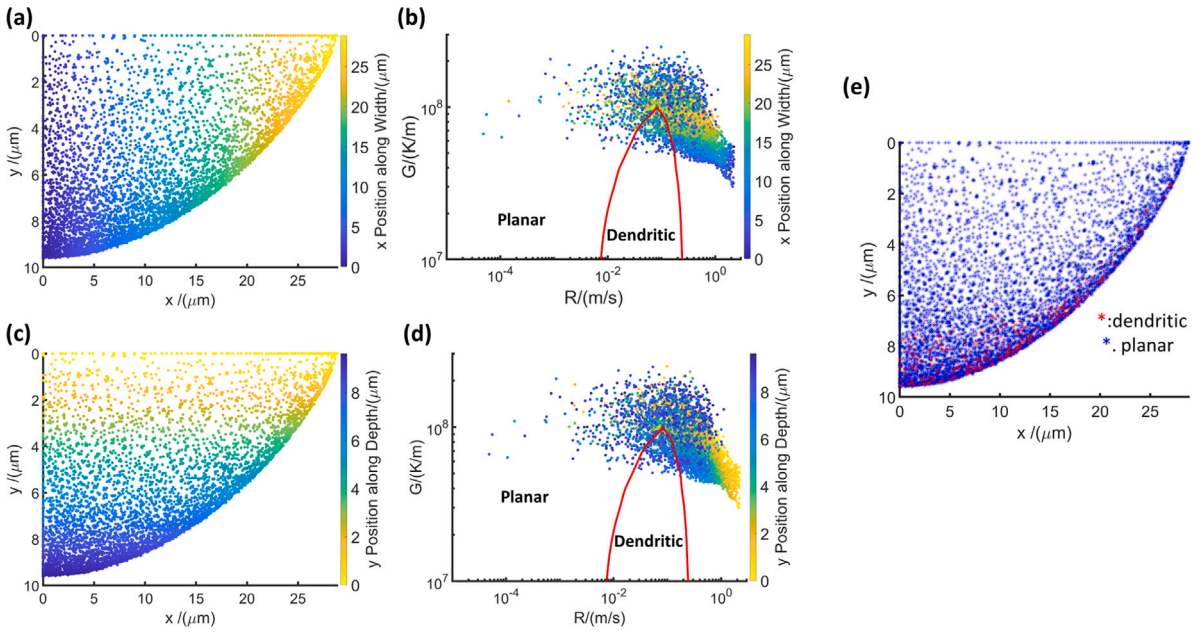


**Fig. 3.** *Fully Planar Microstructure Distribution (low LED condition):* This figure shows the relationship between the color (G, R) and microstructure morphologies (planar and dendritic) in a sample. Panel (a) shows the relationship between color and position along the width direction (x), as depicted in panel (b). In panel (b), the position-dependent G and R are shown, along with the thermal-histories-associated microstructure morphologies. Similarly, panel (c) shows the relationship between color and position along the depth direction (y), as depicted in panel (d). In panel (d), the position-dependent G and R and the thermal-histories-amicrostructure morphologies are shown. The red lines in panels (b) and (d) indicate the boundary between planar and dendritic microstructures on the (G, R) space. The predicted microstructure distribution under a low LED condition (P = 94 W, $|\vec{V}|$ = 2260 mm/s, LED = 41.59 J/m) is shown in panel (e). The planar microstructure is predicted when (G, R) is within the red line, while the dendritic microstructure is obtained outside the line.

$|\vec{V}|$ = 2260 mm/s, and LED = 41.59 J/m. Most of the points in Fig. 3(b) and (d) are located in the planar region since, in the low LED case, R at the melt pool front is large due to the fast $\vec{V}$ in Eq. (8). Under these rapid solidification conditions, the microstructure has insufficient time to evolve stable dendritic growth patterns. The predicted FD value for the track is 0.0045, indicating that the predicted microstructure distribution type for the track is fully planar. Based on OM images, the melt pool width is 68.4 ± 21.1 μm, and the depth is 4.8 ± 3.4 μm experimentally. The predicted melt pool dimension by the integrated model is 57.7 μm in width and 9.62 μm in depth. The predicted melt pool width is consistent with the experimental result, while the predicted melt pool depth is slightly larger than the experimental result.

In Fig. 4, we study the microstructure distribution in a melt pool created with intermediate values for LED (P = 71 W, $|\vec{V}|$ = 300 mm/s and LED = 236.67 J/m). Fig. 4(b) and (d) show position-dependent thermal histories (G and R) predictions across the longitude cross-section. The colors in Fig. 4(b) correspond to the $x$ coordinate along the width direction, and the relative position in the melt pool cross-section can be matched in Fig. 4(a). Similarly, the colors in Fig. 4(d) correspond to the $y$ coordinate along the width direction, and the relative position in the melt pool cross-section can be matched in Fig. 4(c). Based on OM images, the experimental melt pool width is found to be 85.9 ± 0.9 μm, and the depth is 19.8 ± 3.2 μm. The integrated model predicts melt pool dimensions of 77.6 μm in width and 17.1 μm in depth. These predicted melt pool dimensions agree with the experimental results.

As in the case of the low LED case shown in Fig. 3, we can use this visualization scheme to understand the resulting microstructure distribution. In contrast to that case, a larger number of locations within the cross-section of the melt pool is located within the region enclosing the stable dendrite growth regime. This suggests that under these processing conditions, dendrites would form more readily. Yet, other locations within the melt pool are well within the planar growth region. In contrast to the low LED case, the local cooling conditions correspond to low $R$ based on Eq. (8), and in this case, a planar growth microstructure results from the slow evolution of the solid/liquid interface, corresponding to low solidification driving forces, suppressing in turn dendrite growth.

Observing the figure more closely, we can see that the blue markers in Fig. 4(b) correspond to points located at the midpoint of the melt pool. Additionally, the blue markers in Fig. 4(d) correspond to the bottom of the melt pool, as indicated by the link between these colors and the $y$ position shown in Fig. 4(c). Many of these points are located within the stable dendrite growth regime ($0.01 < R < 0.2$ m/s, $G < 10^8$ K/m), suggesting that dendrite growth is likely to occur at the bottom of the melt pool. On the other hand, in Fig. 4(d), yellow markers tend to be in the planar regime because their local $R$ is so fast ($R > 0.2$ m/s) that dendrites do not have sufficient time to form. These yellow markers correspond to the top of the melt pool, as shown in Fig. 4(c).

By mapping locations to the $G - R$ maps, we can determine the microstructure distribution throughout the melt pool. The predicted FD by the integrated model is 0.6341, showing that both planar and dendritic morphologies exist in the melt pool. Fig. 4(e) shows a bottom-dendritic microstructure distribution under medium LED processing conditions, which is consistent with the SEM result in Fig. 4(f). Due to the medium $\vec{V}$, R under these medium LED conditions is lower than that of the low LED case. The lower R results in the top-central region of the melt pool becoming planar. In contrast, the local solidification conditions at the bottom of the melt pool are mostly located within the stable dendrite region in the $G-R$ map, as shown previously in Fig. 4(b) and (d).

Compared with the low LED case, where the fully planar microstructure can be observed, the formation of the dendritic microstructure occurs with the medium and high LED cases. In this medium LED case (P = 71 W, $|\vec{V}|$ = 50 mm/s, LED = 1420 J/m), we find that the blue markers in Fig. 5(b) and yellow markers in Fig. 5(d) correspond to points located at the center of the melt pool. The G-R values for these points have a moderate R ($0.2 > R > 0.01$ m/s) and are located in the dendritic region, so we expect to see only dendritic microstructures at this location. The blue markers in Fig. 5(b) and yellow markers in Fig. 5(d) indicate that the points are located at the bottom of the melt pool. Because the G-R values for most of these points have a small R ($R < 0.01$ m/s) and are located in the planar region, we expect to

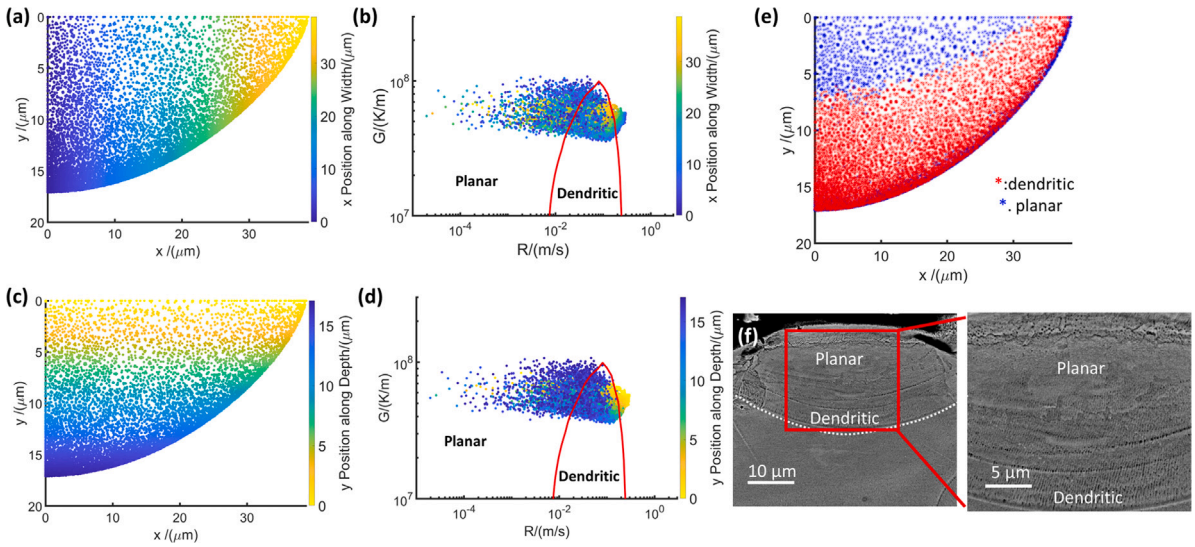


**Fig. 4.** *Bottom Dendritic Microstructure Distribution (medium LED condition):* This figure illustrates the relationship between the microstructure distribution and position-dependent thermal histories in a melt pool under medium LED conditions (P = 71 W, $|\vec{V}|$ = 300 mm/s, LED = 236.67 J/m). (a) Shows the relationship between color and position along the width direction in (b). (b) Displays the position-dependent (x along the width direction) G and R and the corresponding microstructure morphologies (planar and dendritic) based on the thermal histories. (c) Shows the relationship between color and position along the depth direction in (d). (d) Displays the position-dependent (y along the depth direction) G and R, as well as the corresponding microstructure morphologies (planar and dendritic) based on the thermal histories. (e) Predicts the microstructure distribution. (f) Shows the corresponding SEM results of the microstructure distribution under these medium LED conditions. The white dot line in (f) shows the melt pool boundary. The red lines in (b) and (d) indicate the boundary between planar and dendritic microstructures in the (G, R) space. Microstructures are predicted to be planar when (G, R) falls within the line and dendritic otherwise.

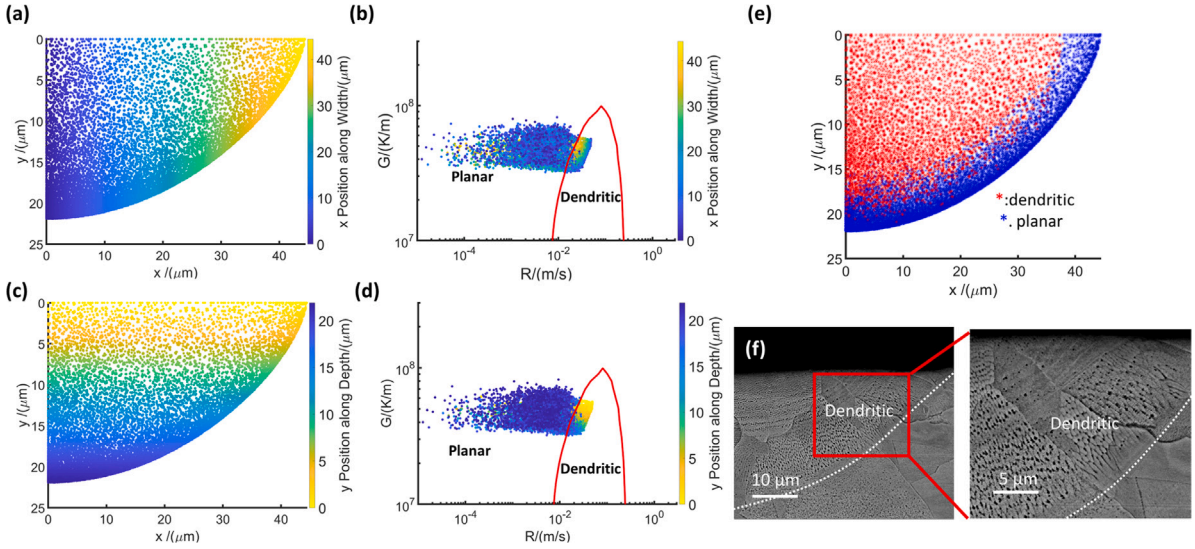


**Fig. 5.** *Top Dendritic Microstructure Distribution (medium LED condition):* This figure presents the relationship between microstructure morphology and G in the width and depth directions during a processing condition of 71 W laser power, 50 mm/s laser velocity and 1420 J/m LED. In panels (b) and (d), the position-dependent G and R are plotted, with the red lines indicating the boundary between planar and dendritic microstructures on the (G, R) space. Panel (e) shows the predicted microstructure distribution based on these relationships, while panel (f) presents the corresponding scanning electron microscopy results. The white dot line in (f) shows the melt pool boundary. The relationship between the color and position in panels (a) and (c) corresponds to the data plotted in panels (b) and (d), respectively.

see a dominant planar microstructure at the bottom of the melt pool. Fig. 5(e) shows a predicted top-dendritic microstructure distribution. The predicted FD of the processing parameter is 0.7067, indicating the majority of the melt pool forms the dendritic microstructure. When $\vec{V}$ is further decreased, the entire (G, R) distribution shifts toward the side with a lower R compared to the previous medium LED case. As a result, the dendritic pattern begins to form at the top-central part, while the bottom part of the melt pool forms a planar microstructure. According to OM images, the experimental melt pool width measures 94.2±8.3 μm, and the depth is 29.3 ± 4.3 μm. The integrated model predicts melt pool dimensions of 88.8 μm in width and 21.9 μm in depth. The predicted melt pool width aligns well with the experimental result, while the predicted depth is smaller than the observed value.

There is some difference between the simulated and predicted results in Fig. 5, with the simulation showing a top-dendritic microstructure distribution with parameters P = 71 W and $|\vec{V}|$ = 50 mm/s in Fig. 5(e), while the SEM images in Fig. 5(f) show a fully-dendritic microstructure. However, it is essential to note that the processing condition depicted in Fig. 5(e) is close to the boundary between mixed and fully dendritic growth patterns, and as such, it is not unexpected to see some deviation between the simulated and experimental results. Nonetheless, FD in Fig. 5(e) is greater than 0.8, indicating that over 80% of the melt pool has the dendritic microstructure. Therefore, the

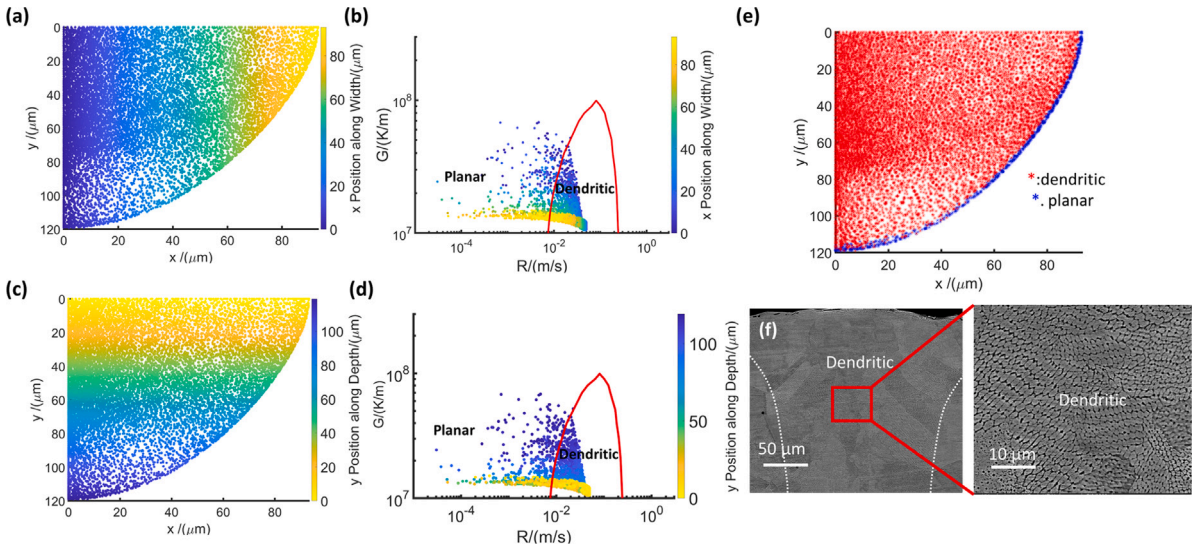


**Fig. 6.** *Fully Dendritic Microstructure Distribution (high LED condition):* This figure presents the relationship between microstructure morphology and G during a high LED processing condition (P = 212 W, $|\vec{V}|$ = 50 mm/s, LED = 4240 J/m). The position-dependent G and R are plotted in panels (b) and (d), respectively, with the red lines indicating the boundary between planar and dendritic microstructures on the (G, R) space. Based on these relationships, the predicted microstructure distribution is shown in panel (e), and the corresponding scanning electron microscopy results are displayed in panel (f). The white dot line in (f) shows the melt pool boundary. The relationship between the color and position in panels (a) and (c) corresponds to the data plotted in panels (b) and (d), respectively.

model can accurately predict the dominant microstructure of the melt pool. When considering the entire processing space, there is overall good agreement between the predicted and experimentally determined microstructure heterogeneity.

In Fig. 6, we examine the microstructure distribution across the cross-section of a melt pool produced under high LED conditions (P = 212 W, $|\vec{V}|$ = 50 mm/s, LED = 4240 J/m). The panels in this figure show that most points fall within the stable dendritic growth regime (panels b and d). As a result, the microstructure distribution predicted in panel (e) indicates that the entire cross-section of the melt pool will solidify into a dendritic structure, confirmed by the scanning electron microscopy image in panel (f). The high laser power, in this case, leads to a lower G. At the same time, the moderate R provides a solidification driving force that is strong enough to encourage the growth of solid/liquid instabilities without being so fast as to suppress dendritic formation. The predicted FD is 0.9863, presenting that the microstructure distribution type for the processing parameters is fully dendritic. Based on the OM images, the experimental melt pool width is 353.3±17.6 μm, and the depth is 409.3±22.4 μm. The integrated model predicts a melt pool dimension of 186 μm in width and 119 μm in depth. The discrepancy between the predicted melt pool dimensions and the experimental results can be attributed to the absence of fluid flow mechanisms in the FE thermal model. Since the processing parameter is located in the keyhole region in Fig. 7b, the fluid flow effect can be dominant.

The analysis presented above for four locations in the processing space suggests that the average cooling rate decreases with increasing LED, and high LED values result in (G, R) combinations that promote the onset of dendritic growth. By performing a similar analysis across the entire processing space, it is possible to gain a more comprehensive understanding of the effect of processing conditions on the extent of microstructure heterogeneity, which arises from the complex interdependence between process parameters and local cooling conditions, as shown in Fig. 7.

The microstructure printability map in Fig. 7(a) presents the area fraction containing the dendrite microstructures (FD) in cross-sections of the melt pool as a function of the processing parameters for the Ni-20 at.%Cu alloy. This map was generated using an integrated model combining the FE thermal model and the finite interface dissipation PFM and is displayed with five contour lines (FD = 0.1/0.3/0.5/0.7/0.9) indicated as black lines. The predictions of the map are validated by experimental measurements of 46 single tracks, which are plotted and classified into four microstructure distribution types: fully planar (purple points), top dendritic (red points), bottom dendritic (black points), and fully dendritic (white points). Fig. 7(c) shows OM images and the corresponding WDS images of typical planar and dendritic microstructure morphologies.

The microstructure printability map in Fig. 7(a) indicates that at $|\vec{V}| > 800$ mm/s, fully planar microstructures are expected to be observed in the cross-sections of the melt pool. This is due to the rapid solidification of the system, which does not allow enough time for dendritic growth instabilities to develop and results in a homogeneous microstructure. On the other hand, at lower laser speeds ($|\vec{V}| \leq 800$ mm/s), a mixture of planar and dendritic structures is observed experimentally and computationally. When the laser speed is low ($|\vec{V}| < 500$ mm/s), dendritic-dominant microstructures are represented for the cross-sections of the melt pool, this is because high laser energy density (LED) melt pools have lower cooling rates ($G * R$), as shown in Fig. 6. As LED increases, the average cooling rate decreases and the combination of (G, R) values that favor dendritic segregation is obtained. The condition, $FD = 0.5$, is used to establish a boundary between planar-dominant and dendritic-dominant microstructures, which is indicated by the solid black line with the label 0.5 in Fig. 7(a). As shown in Fig. 7(a), experimental results are consistent with the simulations, showing only dendritic microstructures observed at low laser speeds ($|\vec{V}| < 500$ mm/s) and only planar microstructures occurring experimentally at higher laser speeds ($|\vec{V}| > 800$ mm/s). The microstructures of the single track transits from a planar pattern to a dendritic pattern with increased LED. All prints with fully dendritic microstructures observed in the experimental results are predicted to be in the dendritic-dominant microstructure region.

Setting an appropriate threshold for the area fraction of predicted dendrite structures (FD) makes it possible to distinguish between heterogeneous and homogeneous microstructure types. In the experiment, 46 microstructure types were observed, with 32 out of 46 identified as fully planar. These cases are indicated by purple symbols in Fig. 7(a). By choosing the right threshold, it may be possible to predict the onset of microstructure heterogeneity consistent with experiments—for instance, setting a threshold of 0.3 results in 4 out of 46 cases being misclassified, or an 8.7% discrepancy. Slightly higher disagreement

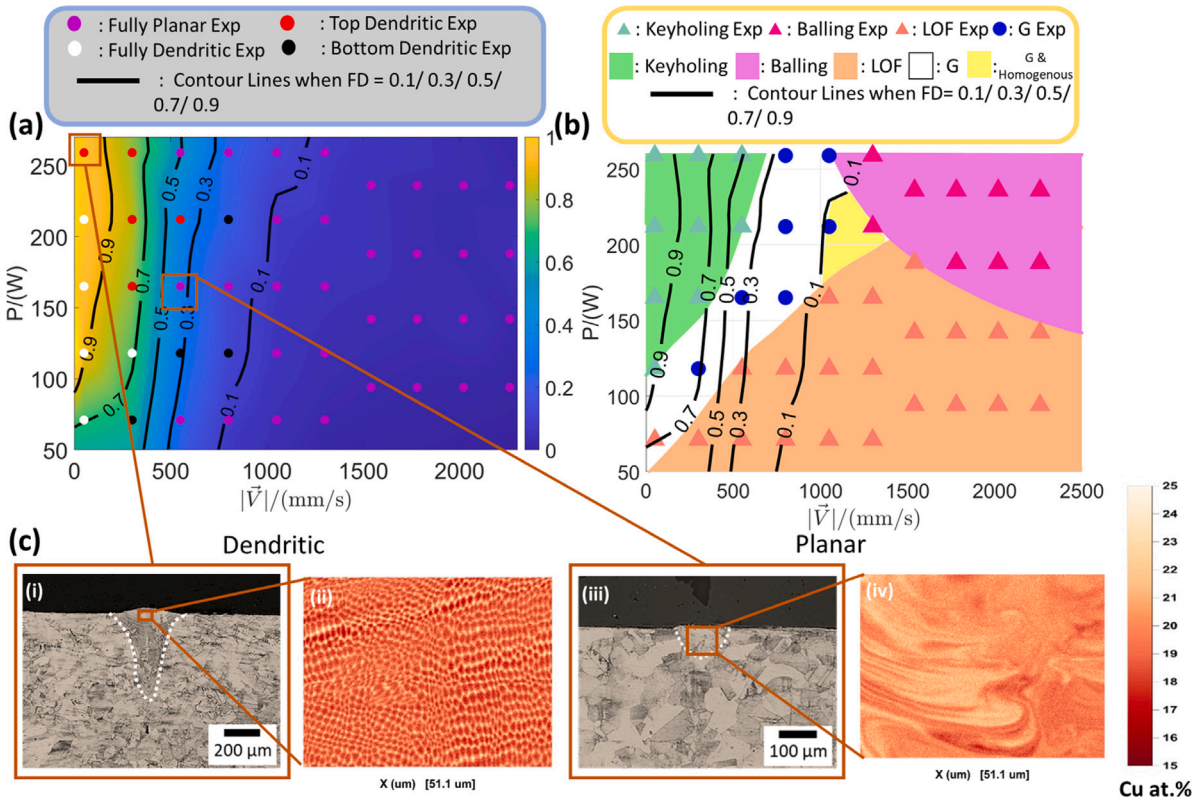


**Fig. 7.** Figure (a) presents a microstructure printability map for LPBF Ni-20 at.%Cu, displaying the area fraction where the dendritic pattern is observed (FD) across the cross-section in relation to the processing parameter in single track scans. The solid black line indicates the boundary where FD is 0.1/0.3/0.5/0.7/0.9, and the purple, red, white, and black points represent experimentally observed fully planar, top dendritic, fully dendritic, and bottom dendritic microstructures, respectively. Figure (b) shows a defect printability map for Ni-20 at.%Cu during LPBF, displaying the types of defects across the processing space. The markers represent the single-track defects observed experimentally across the power–velocity space, including keyholing (green triangle), lack of fusion (orange triangle), and balling (magenta triangle). The blue circles represent good prints that were experimentally obtained, and the green, magenta, orange, and white regions indicate the keyholing, balling, lack of fusion (LOF), and good processing regions predicted by the Eagar–Tsai model in Seede et al.'s work [17]. The yellow region represents the predicted processing parameter region that leads to a homogeneous, dendrite- and defect-free microstructure. Within this region, this alloy is predicted to be *unconditionally printable*. Figure (c) displays two OM images with the corresponding processing parameters shown on the map. The wavelength dispersive spectroscopy (WDS) images on the right indicate the Cu compositional distribution of two single-track scans. These maps illustrate the characteristic dendritic and planar morphology predicted in single-track scans under varying processing parameters.

is observed when FD is set to 0.1, leading to 6 out of 46 cases, or 13%, being misaligned with the experimental results. However, a prediction of FD = 0.1 indicates that at least 90% of the melt pool cross-section would correspond to a planar microstructure, and all the processing parameter predicted to have the fully planar is consistent with experiments. Therefore, to obtain a homogeneous microstructure, selecting FD equal to 0.1 is recommended, as it will not misclassify a heterogeneous microstructure. Furthermore, since more than 90% of the whole melt pool area shows a planar pattern, the microstructure in the melt pool is nearly homogeneous.

Note that the experimental microsegregation conditions are only investigated in the melt pool's top, bottom, and edge parts. This limited observation may result in an underestimation of the dendritic area fraction, as the whole melt pool front is not fully observed. As per our analysis, one out of 32 single tracks printed as fully planar on the printability map, the experimentally observed microstructure was predicted to be dendritic-dominant. However, this point is located on the boundary between planar-dominant and dendritic-dominant microstructures.

The discrepancy between the predictions and experiments in this region of the processing space may be due to variance in the solidification conditions along the length of the melt pool. The complicated solidification environment at the melt pool front can result in different microstructure distributions in the longitude cross sections taken at different locations for the same single track. Additionally, the FE thermal model used in this work did not consider fluid flow effects, which may significantly impact the solidification process in high-LED process regions.

By combining the microstructure printability map in Fig. 7a with the defect printability map, the defect-free and microstructure-homogeneous region can be predicted in the processing parameter space. Fig. 7b shows the defect printability map predicted by the Eagar–Tsai model in Seede et al.'s work [17]. This map displays the processing parameter regions where three types of macroscopic defects are predicted to occur: keyholing (green), lack of fusion (orange), and balling (magenta). The corresponding experimental data points are shown in the same colors as the predicted regions, and the blue points represent the process parameters in which good prints without macroscopic defects were obtained experimentally. The keyholing criterion is $W/D \leq 1.2$ and the lack of fusion criterion is $D \leq 0.667$, where $W$ corresponds to the melt pool width and $D$ is the melt pool depth. A support Vector Machine (SVM) classifier was used to predict the balling region based on experimental results [17]. In their work, A third-degree polynomial kernel support vector machine (SVM) classifier was employed to identify the balling region for each material. After establishing these defect criteria, finalized processing maps can be created for each alloy [53]. In Fig. 7b, the solid black line indicates the location where FD is 0.1/0.3/0.5/0.7/0.9, which represents the predicted boundary between the heterogeneous and homogeneous microstructure with varying thresholds in the processing parameter space.

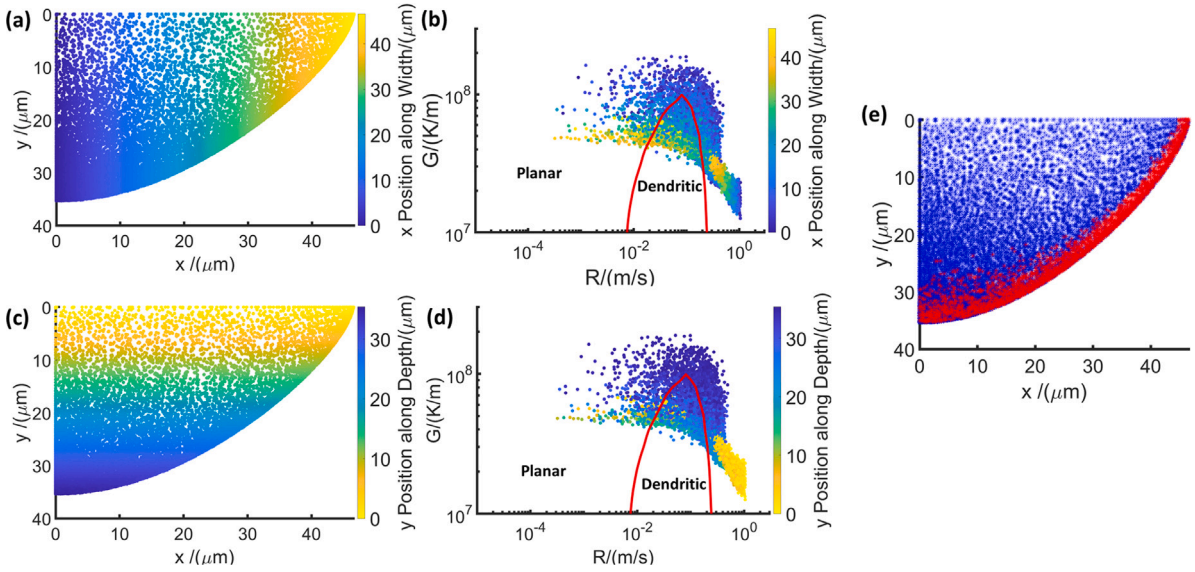


**Fig. 8.** *Microstructure Distribution at unconditionally printable regime:* This figure presents the relationship between microstructure morphology and G in the width and depth directions during a processing condition of 212 W laser power, 1050 mm/s laser velocity, and 201.9 J/m LED. This processing condition corresponds to the small yellow region in Fig. 7(b). In panels (b) and (d), the position-dependent G and R are plotted, with the red lines indicating the boundary between planar and dendritic microstructures on the (G, R) space. Panel (e) shows the predicted microstructure distribution based on these relationships. The relationship between the color and position in panels (a) and (c) corresponds to the data plotted in panels (b) and (d), respectively. FD is 0.083, indicating a mostly planar microstructure with minimal microsegregation.

By comparing Fig. 7(a) and Fig. 7(b), it is evident that there is only a small region in the processing space, indicated by the yellow color in Fig. 7(b), where fully homogeneous microstructures can be expected in the printable region of the processing space for LPBF. This result is significant because it indicates that, for this alloy, there are intrinsic limits to the ability to print defect-free homogeneous microstructures. The dendritic microstructure can be identified as a significant contributor to certain defects, such as hot cracking [54,55]. The yellow region corresponds to the *unconditionally printable regime*, in which parts can be printed that would require no post-processing to homogenize the microstructure. In contrast, a significant portion of the printable region for this system would result in microstructures dominated by dendritic growth patterns.

The microstructure distribution and corresponding local thermal history at a set of processing conditions within the unconditionally printable regime (yellow region in Fig. 7(b)) are shown in Fig. 8. As shown in Fig. 8(b) and (d), the majority of the local thermal histories in the (G, R) map are located within the planar region, resulting in a primarily planar microstructure throughput the melt pool cross-section as shown in Fig. 8(e). According to the OM images, the experimental melt pool width is 102.6 ± 2.1 μm and the depth is 51.6 ± 8.6 μm. The integrated model predicts a melt pool dimension of 101 μm in width and 48.1 μm in depth, which agrees with the experimental results. The predictions suggest that only a tiny region at the bottom of the melt pool is likely to solidify as a dendritic microstructure with microsegregation. The computed FD for this particular condition is 0.07, which is below the 0.1 that we observed was the threshold to predict an experimentally observed melt pool cross-section consisting of exclusively planar growth solidification microstructures. Within this regime, increasing $|\vec{V}|$ could potentially move the entirety of the local (G, R) conditions within the melt pool to the (fast) planar growth regime, but at these $|\vec{V}|$ it is likely that balling defects would form. On the other hand, decreasing $|\vec{V}|$ would move (G, R) conditions within the melt pool to the (slow) planar growth regime. However, under these conditions, it is likely that the LED would be so high that keyhole porosity would be observed. This suggests that control of the melt pool thermal history to minimize microsegregation may be possible but quite challenging in practice, particularly considering that the thermal histories, under the same nominal process settings, may actually change quite significantly depending on the local cooling conditions.

We note once again that this alloy has a relatively narrow solidification range of approximately 20 K, which is comparable to the solidification range of many alloys currently being investigated for AM applications. However, it is expected that the vast majority of a given alloy space will have significantly higher solidification ranges. While the onset of dendrite growth is also strongly influenced by other thermophysical properties such as thermal conductivity and mass diffusivities in both solid and liquid phases, the solidification range, $\Delta T$, is a dominant factor: as $\Delta T$ increases, the region in the G-R map corresponding to stable dendrite growth expands accordingly.

Although it may be difficult to find processing conditions that simultaneously eliminate both macroscopic defects and microscopic heterogeneities within alloy spaces of interest to the AM community, it is not impossible. Finding a solution to this challenge could bring significant advancements in the process science for AM and lead to even greater possibilities in the field. Additionally, the potential impacts of the top, bottom, and fully dendritic microstructure distributions needs future investigation."

## 5. Conclusion

In this study, we used an integrated model combining phase field and thermal models to predict the microstructure distribution in a model Ni–Cu binary alloy under low, medium, and high LED conditions. The resulting melt pool cross-sections were observed to belong to four major categories: fully planar, bottom dendritic, top dendritic, and fully dendritic. These different microstructures were found to be the result of different cooling conditions and locations in the G-R maps. By combining the microstructure printability map with a process printability map, we were able to identify a narrow region in the processing space known as the *unconditionally printable regime*, where little or no post-processing is necessary to achieve parts that are porosity-free and have homogeneous microstructures. The major findings of the present work can be summarized as follows:

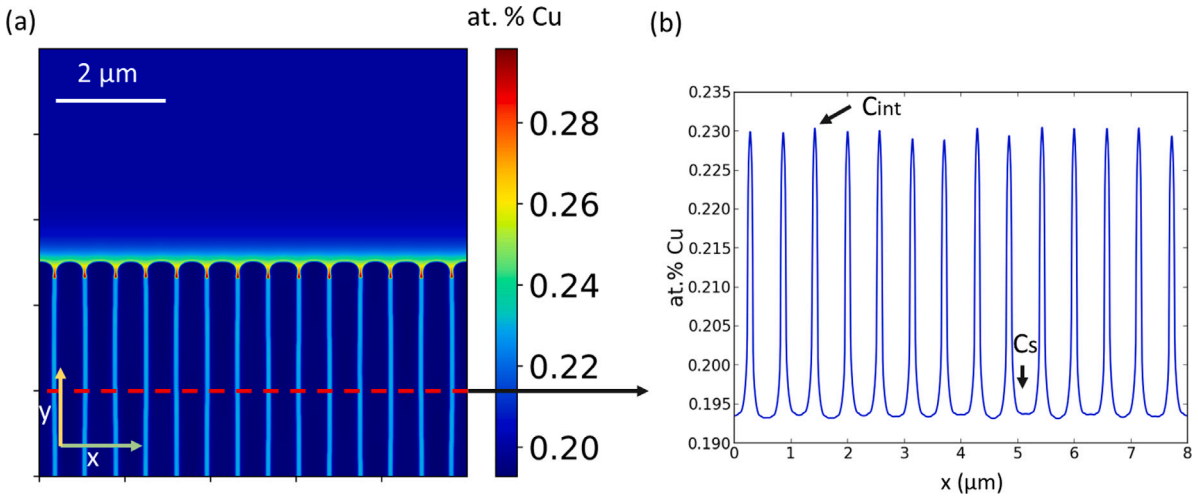


**Fig. A.1.** (a) Typical dendritic microstructure forms under L-PBF condition by FID model (G = 3.2 × $10^7$ K/m, R = 0.0126 m/s). Cu concentration varies along line *x* axis (b).

1. In the Ni-20 at.% Cu alloy system, we observed four different microstructure distribution types under low, medium, and high LED conditions. Experimentally and computationally, we found that low LED conditions result in a fully planar microstructure distribution. However, as LED is increased, dendritic growth patterns tend to form at the bottom of the melt pool. As LED increases even further, the location of dendrite growth shifts to the top of the melt pool. At very high LED levels and low scan velocities, we observe fully dendritic microstructures.

2. The thermal history distribution at the melt pool front has a strong correlation with the distribution of the microstructure across the melt pool. When the LED is high, the local cooling rate at the melt pool front tends to be low, which causes the formation of the dendritic microstructure.

3. A microstructure printability map was created for Ni-20 at.%Cu under L-PBF AM conditions using an integrated model coupling phase field and thermal models. The map was used to predict the dendritic and planar microstructure distribution under various solidification conditions across the laser power-scan velocity processing parameter space, based on the dendritic area fraction. These predictions were validated by experimental results.

4. The microstructure printability map was also used to predict the homogeneous and heterogeneous microstructure distribution under various solidification conditions across the laser power-scan speed parameter space. Homogeneity was defined as a fully planar microstructure with no microsegregation. The simulated results were found to match the experimental results well.

5. By combining the microstructure printability map with a defect printability map predicted by the Eagar–Tsai model, it was possible to identify a region in the processing space that corresponds to the 'unconditionally printable regime', in which it is possible to obtain both microstructure-homogeneous and defect-free prints. This regime can be used to avoid costly post-processing.

6. The relatively narrow solidification range of approximately 20 K in the Ni-20 at.%Cu alloy system is similar to that of many commonly printed alloys. However, the fact that an alloy with such a narrow solidification range has a small unconditionally printable regime suggests that it may be challenging to find alloys with wide unconditionally printable regimes in practice.

## CRediT authorship contribution statement

**Xueqin Huang:** Conceptualization, Methodology, Software, Formal analysis, Writing – original draft. **Raiyan Seede:** Experiment, Formal analysis, Writing – original draft, Writing – review & editing. **Kubra Karayagiz:** Methodology, Formal analysis, Writing – review & editing. **Austin Whitt:** Experiment, Formal analysis, Writing – review & editing. **Bing Zhang:** Experiment, Formal analysis, Writing – review & editing. **Jiahui Ye:** Experiment, Formal analysis, Writing – review & editing. **Ibrahim Karaman:** Supervision, Conceptualization, Methodology, Formal analysis, Writing – review & editing, Funding acquisition. **Alaa Elwany:** Supervision, Conceptualization, Methodology, Formal analysis, Writing – review & editing, Funding acquisition. **Raymundo Arróyave:** Supervision, Conceptualization, Methodology, Formal analysis, Writing – review & editing, Funding acquisition.

## Declaration of competing interest

The authors declare that they have no known competing financial interests or personal relationships that could have appeared to influence the work reported in this paper.

## Data availability

Data will be made available on request.

## Acknowledgments

This work was carried out with support from the Army Research Office (ARO) under Contract No. W911NF-18-1-0278 and support from the National Science Foundation (NSF) Award No. 1846676. XH, KK, and RA also acknowledge Lawrence Livermore National Laboratory under Collaborative R&D in Support of LLNL Missions, Task Order No. B623252 and Master Task Agreement. The FE and PFM simulations were performed at the Texas A&M Super Computing Center.

## Appendix

See Figs. A.1–A.3.

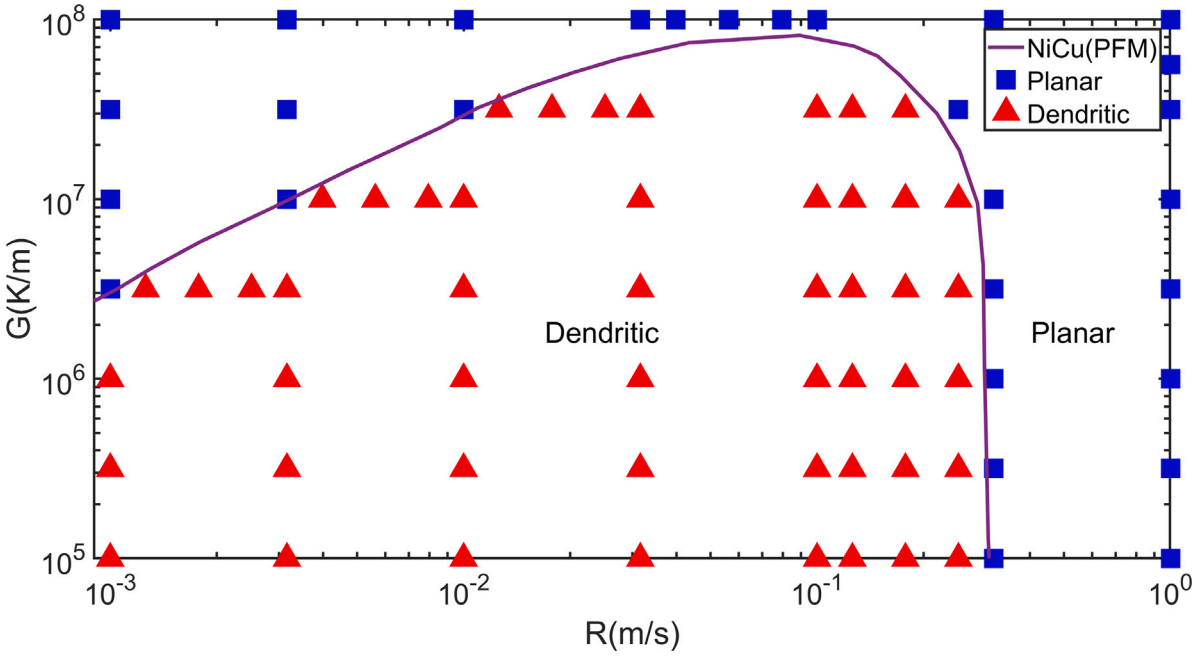


**Fig. A.2.** The (G, R) Combinations used to generate the dendritic-planar boundary predicted by PFM. The blue point indicates that the planar microstructure was predicted by PFM. The red point shows that the dendritic microstructure was predicted by PFM. The purple line represents the boundary between the dendritic microstructure and planar microstructure predicted by PFM.

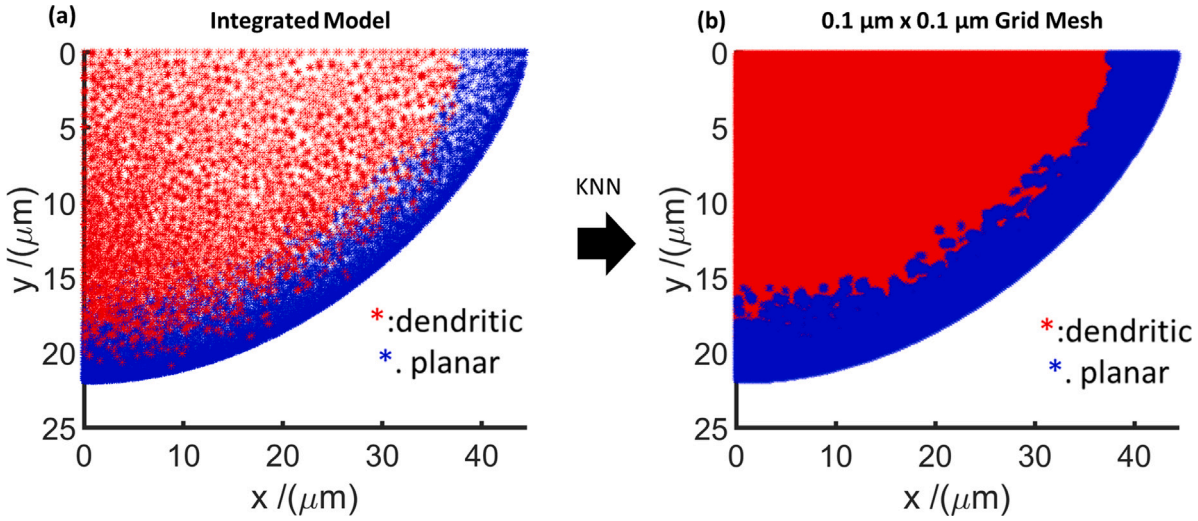


**Fig. A.3.** The microstructure morphology predicted (a) by the integrated Model and (2) on 0.1 μm × 0.1 μm based by KNN.

## References


[1] W. Frazier, Metal additive manufacturing: A review, J. Mater. Eng. Perform. 23 (2014) 1917–1928.

[2] T. DebRoy, et al., Additive manufacturing of metallic components–process, structure and properties, Progr. Mater. Sci. 92 (2018) 112–224.

[3] D. Brackett, I. Ashcroft, R. Hague, Topology optimization for additive manufacturing, in: Proceedings of the solid freeform fabrication symposium, Austin, TX, Vol. 1, 2011, pp. 348–362.

[4] T. Zegard, G. Paulino, Bridging topology optimization and additive manufacturing, Struct. Multidiscip. Optim. 53 (2016) 175–192.

[5] W. Gao, et al., The status, challenges, and future of additive manufacturing in engineering, Comput.-Aided Des. 69 (2015) 65–89.

[6] T. Ngo, A. Kashani, G. Imbalzano, K. Nguyen, D. Hui, Additive manufacturing (3D printing): A review of materials, methods, applications and challenges, Compos. B Eng. 143 (2018) 172–196.

[7] H. Lee, et al., Lasers in additive manufacturing: A review, Int. J. Precis. Eng. Manuf.-Green Technol. 4 (2017) 307–322.

[8] M. Seifi, A. Salem, J. Beuth, O. Harrysson, J. Lewandowski, Overview of materials qualification needs for metal additive manufacturing, JOM 68 (2016) 747–764.

[9] J. Lewandowski, M. Seifi, Metal additive manufacturing: A review of mechanical properties, Annu. Rev. Mater. Res. 46 (2016) 151–186.

[10] G. Tapia, et al., Uncertainty propagation analysis of computational models in laser powder bed fusion additive manufacturing using polynomial chaos expansions, J. Manuf. Sci. Eng. 140 (2018).

[11] R. Acharya, J. Sharon, A. Staroselsky, Prediction of microstructure in laser powder bed fusion process, Acta Mater. 124 (2017) 360–371.

[12] T. Keller, et al., Application of finite element, phase-field, and calphad-based methods to additive manufacturing of ni-based superalloys, Acta Materialia 139 (2017) 244–253.

[13] Y. Arısoy, et al., Influence of scan strategy and process parameters on microstructure and its optimization in additively manufactured nickel alloy 625 via laser powder bed fusion, Int. J. Adv. Manuf. Technol. 90 (2017) 1393–1417.

[14] X. Zhang, W. Ye, L. Mushongera, Y. Liao, Unravelling heterogeneities in sub-grain cellular structure and micromechanical response of additive manufactured Ti-Nb alloys, Addit. Manuf. (2022) 103146.

[15] J. Berry, et al., Toward multiscale simulations of tailored microstructure formation in metal additive manufacturing, Mater. Today 51 (2021) 65–86.
[16] Z. Liu, et al., Additive manufacturing of metals: Microstructure evolution and multistage control, J. Mater. Sci. Technol. 100 (2022) 224–236.
[17] R. Seede, et al., Effect of composition and phase diagram features on printability and microstructure in laser powder bed fusion: Development and comparison of processing maps across alloy systems, Addit. Manuf. 47 (2021) 102258.
[18] F. Yu, Y. Wei, Y. Ji, L.-Q. Chen, Phase field modeling of solidification microstructure evolution during welding, J. Mater Process. Technol. 255 (2018) 285–293.
[19] L. Nastac, Numerical modeling of solidification morphologies and segregation patterns in cast dendritic alloys, Acta Mater. 47 (1999) 4253–4262.
[20] Q. Xu, et al., Multiscale modeling and simulation of directional solidification process of ni-based superalloy turbine blade casting, Metals 8 (2018) 632.
[21] M. Zaeem, H. Yin, S. Felicelli, Modeling dendritic solidification of Al–3% Cu using cellular automaton and phase-field methods, Appl. Math. Model. 37 (2013) 3495–3503.
[22] A. Karma, D. Tourret, Atomistic to continuum modeling of solidification microstructures, Curr. Opin. Solid State Mater. Sci. 20 (2016) 25–36.
[23] V. Attari, R. Arroyave, Phase field modeling of joint formation during isothermal solidification in 3DIC micro packaging, J. Phase Equilibria Diffus. 37 (2016) 469–480.
[24] V. Attari, S. Ghosh, T. Duong, R. Arroyave, On the interfacial phase growth and vacancy evolution during accelerated electromigration in Cu/Sn/Cu microjoints, Acta Mater. 160 (2018) 185–198.
[25] J. Pauza, A. Rollett, Simulation study of hatch spacing and layer thickness effects on microstructure in laser powder bed fusion additive manufacturing using a texture-aware solidification potts model, J. Mater. Eng. Perform. 30 (2021) 7007–7018.
[26] J. Pauza, W. Tayon, A. Rollett, Computer simulation of microstructure development in powder-bed additive manufacturing with crystallographic texture, Modelling Simul. Mater. Sci. Eng. 29 (2021) 055019.
[27] S. Sheikh, et al., An automated fully-computational framework to construct printability maps for additively manufactured metal alloys, 2023, 2304.04113.
[28] S. Sheikh, et al., High-throughput alloy and process design for metal additive manufacturing, 2023, 2304.04149.
[29] L. Johnson, et al., Assessing printability maps in additive manufacturing of metal alloys, Acta Mater. 176 (2019) 199–210.
[30] I. Steinbach, L. Zhang, M. Plapp, Phase-field model with finite interface dissipation, Acta Mater. 60 (2012) 2689–2701.
[31] K. Karayagiz, et al., Finite interface dissipation phase field modeling of Ni–Nb under additive manufacturing conditions, Acta Mater. 185 (2020) 320–339.
[32] X. Wang, et al., Investigation on microsegregation of In718 alloy during additive manufacturing via integrated phase-field and finite-element modeling, J. Mater. Eng. Perform. 28 (2019) 657–665.
[33] S. Sahoo, K. Chou, Phase-field simulation of microstructure evolution of Ti–6Al–4V in electron beam additive manufacturing process, Addit. Manuf. 9 (2016) 14–24.
[34] X. Huang, et al., Hybrid microstructure-defect printability map in laser powder bed fusion additive manufacturing, Comput. Mater. Sci. 209 (2022) 111401.
[35] T. Mukherjee, T. DebRoy, Printability of 316 stainless steel, Sci. Technol. Weld. Join. 24 (2019) 412–419.
[36] P. Nie, O. Ojo, Z. Li, Numerical modeling of microstructure evolution during laser additive manufacturing of a nickel-based superalloy, Acta Mater. 77 (2014) 85–95.
[37] R. Seede, et al., An ultra-high strength martensitic steel fabricated using selective laser melting additive manufacturing: Densification, microstructure, and mechanical properties, Acta Materialia 186 (2020) 199–214.
[38] J. Roehling, et al., Rapid solidification in bulk Ti-Nb alloys by single-track laser melting, JOM 70 (2018) 1589–1597.
[39] D. Fisher, W. Kurz, Fundamentals of solidification, Fundam. Solidif. (1998) 1–316.
[40] R. Trivedi, W. Kurz, Dendritic growth, Int. Mater. Rev. 39 (1994) 49–74.
[41] M. Asta, et al., Solidification microstructures and solid-state parallels: Recent developments, future directions, Acta Materialia 57 (2009) 941–971.
[42] C. Alcock, V. Itkin, M. Horrigan, Vapour pressure equations for the metallic elements: 298–2500k, Canadian Metall. Q. 23 (1984) 309–313.
[43] C. Multiphysics, Comsol Multiphysics Reference Guide, 2011.
[44] D. Laeter, et al., Atomic weights of the elements. Review 2000 (Iupac technical report), Pure Appl. Chem. 75 (2003) 683–800.
[45] T.-C. Software, Thermal-calc TcNi11:Ni-alloys v11.0.1.
[46] C. Smithells, C. Smith, Metals reference book, Phys. Today 8 (1955) 27.
[47] M. Chase, N. (US), NIST-JANAF Thermochemical Tables, Vol. 9, American Chemical Society, Washington, DC, 1998.
[48] L. Zhang, I. Steinbach, Phase-field model with finite interface dissipation: Extension to multi-component multi-phase alloys, Acta Mater. 60 (2012) 2702–2710.
[49] N. Saunders, A. Miodownik, CALPHAD (Calculation of Phase Diagrams): A Comprehensive Guide, Elsevier, 1998.
[50] MATLAB, Version R2020a, The MathWorks Inc, Natick, Massachusetts, 2020.
[51] Y. Yang, et al., Additive manufacturing of Wc-Co hardmetals: A review, Int. J. Adv. Manuf. Technol. 108 (2020) 1653–1673.
[52] C. Singer, M. Schmitt, G. Schlick, J. Schilp, Multi-material additive manufacturing of thermocouples by laser-based powder bed fusion, Procedia CIRP 112 (2022) 346–351.
[53] B. Scholkopf, A. Smola, Learning with Kernels: Support Vector Machines, Regularization, Optimization, and Beyond, MIT press, 2018.
[54] S. Qin, et al., Influence of process parameters on porosity and hot cracking of AISI H13 fabricated by laser powder bed fusion, Powders 1 (2022) 184–193.
[55] W. Stopyra, K. Gruber, I. Smolina, T. Kurzynowski, B. Kuźnicka, Laser powder bed fusion of Aa7075 alloy: Influence of process parameters on porosity and hot cracking, Addit. Manuf. 35, 101270.